Chemical Science

ROYAL SOCIETY OF CHEMISTRY

EDGE ARTICLE

View Article Online
View Journal | View Issue

Cite this: *Chem. Sci.*, 2025, **16**, 7946

All publication charges for this article have been paid for by the Royal Society of Chemistry

Received 28th January 2025
Accepted 26th March 2025

DOI: 10.1039/d5sc00767d

rsc.li/chemical-science

Solvent-free approach for the synthesis of heterometallic Fe–Zn-ZIF glass *via* a melt-quenched process†

Luis León-Alcaide, [a] Celia Castillo-Blas, [b] Vlad Martin-Diaconescu,[c] Ivan da Silva, [d] David A. Keen, [d] Thomas D. Bennett ‡[b] and Guillermo Mínguez Espallargas *[a]

We report the solvent-free synthesis of a crystalline heterometallic imidazolate derivative with formula $[Fe_1Zn_2(im)_6(Him)_2]$, designated **MUV-25**, incorporating both iron and zinc. The structure imposes strict positional constraints on the metal centres due to the lattice containing distinct geometric coordination sites, tetrahedral and octahedral. As a consequence, each metal is exclusively directed to its specific coordination site, ensuring precise spatial organization within the lattice. Atom locations were meticulously monitored utilizing X-ray diffraction (single crystal and total scattering) and XAS techniques, demonstrating that the tetrahedral sites are occupied exclusively by zinc, and the octahedral sites are occupied by iron. This combination of metal centres results, upon heating, in a structural phase transformation to the **zni** topology at a very low temperature. Further heating causes the melting of the solid, yielding a heterometallic MOF-derived glass. The methodology lays the groundwork for tailoring crystalline structures to advance the development of novel materials capable of melting and forming glasses upon cooling.

Introduction

Metal–Organic Framework glasses (**a_g-MOFs**) represent an intriguing class of amorphous materials characterized by their disordered atomic arrangements, similar to traditional glasses.[1,2] However, their composition, based on metal ions or clusters interconnected by organic ligands, establishes them as hybrids between conventional MOFs and glassy materials.[3,4] These glass structures maintain the essence of the original crystalline analogues while showcasing distinctive properties such as a monolithic design,[5] enhanced proton conductivity,[6] thermal conductivity,[7] porosity,[8] mechanical[9] or optical properties.[10–12] In addition, their amorphous nature enables them to circumvent certain limitations faced by their crystalline counterparts, such as limited processability and susceptibility to structural collapse under external stimuli,[13] thus allowing their application in devices (*e.g.*, as electrolytes,[14,15] solar cells,[16] membranes,[17,18] composites[19] or as anodes for Li-ion batteries).[20]

From a mechanistic point of view, the melting of MOFs entails the dynamic breaking and reformation of metal–ligand bonds.[21] However, despite the extensive knowledge in the synthesis of MOFs,[22] only a few of them can be melted to create glassy materials upon cooling.[23–27] The most significant ones belong to one subfamily of MOFs denoted zeolitic imidazolate frameworks (ZIFs),[29] which comprise M^{2+} ions (typically Zn^{2+} and Co^{2+}) linked *via* imidazolate bridges. Some of them are able to melt[30,31] before the typical decomposition process experienced by the vast majority of MOFs,[32] being **ZIF-4** $[Zn(im)_2]$[28] and its derivatives the most significant ones within this family. Quenching the liquid ZIF to room temperature yields a ZIF glass, which retains tetrahedrally coordinated M^{2+} ions with imidazolate linkers but lacks long-range order.[31]

In the particular case of ZIFs, a high percentage of underivatized imidazolate ligands seems to be essential to achieve the melt state.[33] Thus, one possible solution to expand the range of materials capable of melting is to maintain the general structure and subtly modify the network of the crystalline precursor, either in the organic or in the inorganic parts. For instance, incorporating small amounts of bulkier imidazole derivatives, such as benzimidazole, causes a reduction in the melting temperature, as exemplified by **ZIF-62**, $[Zn(im)_{1.75}(bim)_{0.25}]$,[31]

[a]*Instituto de Ciencia Molecular (ICMol), Universidad de Valencia, c/ Catedrático José Beltrán, 2, 46980, Paterna, Spain. E-mail: guillermo.minguez@uv.es*

[b]*Department of Materials Science and Metallurgy, University of Cambridge, Cambridge, CB3 0FS, UK*

[c]*CELLS-ALBA Synchrotron, E-08290 Cerdanyola del Vallès, Barcelona, Spain*

[d]*ISIS Facility, Rutherford Appleton Laboratory, Harwell Campus, Didcot, Oxfordshire OX11 0QX, UK*

† Electronic supplementary information (ESI) available. CCDC 2373266 and 2373267. For ESI and crystallographic data in CIF or other electronic format see DOI: https://doi.org/10.1039/d5sc00767d

‡ Present address: School of Physical and Chemical Sciences, University of Canterbury, Private Bag 4800, Christchurch 8140, New Zealand.

and its derivatives.[34] However, the role of the metal is still rather unexplored and the vast majority of ZIFs are prepared with zinc, and only a few with cobalt.[30,35] Recently, our group has reported the first Fe-ZIF glass, denoted **a$_g$-MUV-24**,[36] which is obtained through multi-structural rearrangements and melts at lower temperatures than the zinc analogue.

Another interest in the area is the preparation of multimetallic glasses. As with their crystalline counterparts, mixed-metal MOFs have been shown as suitable platforms for controlling gas affinity, tuning breathing behaviour, and enabling synergistic catalytic processes.[37] However, the effect of incorporating a second metal into the lattice of a glass, as well as the phase transitions it undergoes, has been scarcely studied. In this sense, the incorporation of cobalt into the zinc-based glassy network slightly lowers the melting temperature.[38] Glasses formed with more than one metal can be prepared by mixing two different crystalline precursors albeit this implies that both of them have to melt at similar temperatures.[39] Alternatively, a uniform glass can result using mixed-metal meltable ZIFs,[40] which is more challenging, but has been primarily used with Co and Zn, as both share the same glass-forming crystalline network topology, **cag**.[41] The main challenge in overcoming this limitation is to identify an initial topology capable of incorporating diverse metals while maintaining enough density to enable subsequent melting, a criterion met only by the **cag** and **zni** topologies.

We have recently reported another topology, **mog**, that facilitates the formation of the **zni** phase with Fe, unachievable by direct conditions.[36,42] This **mog** topology features two distinctly different metal coordination environments—octahedral and tetrahedral—and therefore, could be suitable for the incorporation of metal centres with distinctive chemical affinities. In this work, we use this glass-forming crystalline precursor as a platform for incorporating different metals, while also exploring the influence of the metal ion in the melt-quenching process. To achieve this, we have integrated iron and zinc centres into the **mog** lattice using a solvent-free approach, resulting in a heterometallic imidazolate derivative with restricted constraints on the location of both metals. This heterometallic crystalline material undergoes a transformation into another crystalline phase with the **zni** topology. This thermally activated structural phase transition is one of the few that have demonstrated to be able of melt.[43] Furthermore, this research enables us to explore the effects on melting temperature (T_m) and glass transition (T_g) from incorporating two different metal nodes within the same framework and compare with the pure counterparts.

Results and discussion

The solvent-free reaction of a 1 : 1 : 4 mixture of ferrocene, zinc oxide and imidazole at 150 °C under vacuum yields, after 24 hours, an orange crystalline material that has the **mog** topology, designated as **MUV-25(mog)** (MUV = Material of the University of Valencia). Single crystal X-ray diffraction of the as-synthesized material reveals that **MUV-25(mog)** is a 3D coordination polymer with formula $[M_3(im)_6(Him)_2]$ in which tetrahedral and octahedral metal centres are linked *via* imidazolate bridges, with two tetrahedral sites per octahedral site. Each metal ion is connected to four other metal nodes, with the octahedral centres possessing two terminal imidazole molecules in a *trans*-configuration (see Fig. 1). **MUV-25(mog)** closely resembles the pure iron phase, $[Fe_3(im)_6(Him)_2]$ (CCDC code = IMIDFE)[44] and the pure cobalt phase, $[Co_3(im)_6(Him)_2]$ (CCDC code = OWIGIL),[45] and crystallizes in the same space group ($P2_1/c$) with similar unit cell parameters (a = 10.388 Å, b =

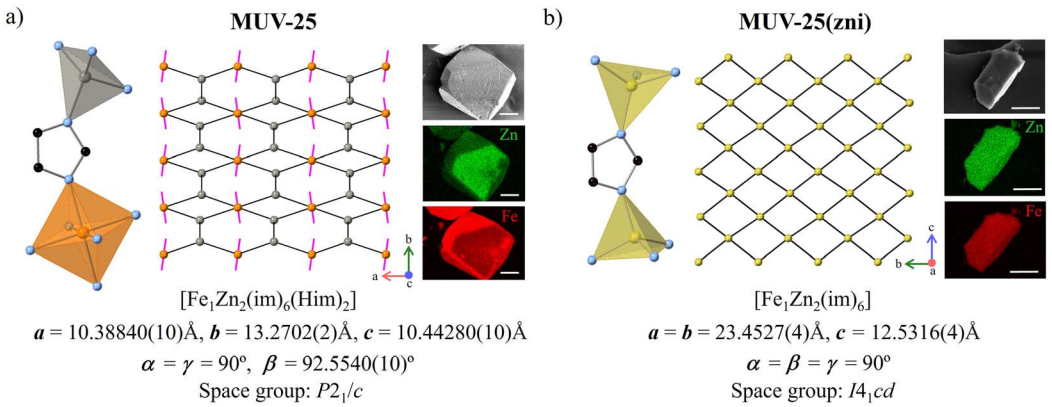

Fig. 1 (a) Crystal structure of **MUV-25(mog)**. (Left) The structure is composed of tetrahedral zinc atoms (in grey) and octahedral iron atoms (in orange) connected *via* imidazolate ligands (nitrogen and carbon atoms are represented as blue and black spheres, respectively). (Middle) Projection of the topology of **MUV-25(mog)**, with the Fe centres shown as orange spheres, Zn centres as grey spheres, the bridging imidazolates as grey lines, and the terminal imidazoles as pink lines. (Right) SEM image of **MUV-25(mog)** and its corresponding elemental mapping of zinc and iron (scale bars = 10 μm). (b) Crystal structure of **MUV-25(zni)**. (Left) The structure is composed of tetrahedral metal atoms (in yellow) with positional iron:zinc disorder, connected *via* imidazolate ligands (nitrogen and carbon represented as blue and black spheres, respectively). (Middle) Projection of the topology of **MUV-25(zni)**, with the metal centres shown as yellow spheres and the bridging imidazolates as grey lines. Note that the single-crystal X-ray data does not differentiate between the metal centres. (Right) SEM image of **MUV-25(zni)** and its corresponding elemental mapping of zinc and iron (scale bars = 10 μm).

13.270 Å, $c = 10.443$ Å, $\beta = 92.554°$). However, it differs significantly from the pure zinc phase obtained through solvent-free synthesis, consisting exclusively of tetrahedral zinc centres, which is the same as previously reported *via* ionothermal synthesis: $[Zn_4(im)_8(Him)]$ (CCDC code = KUMXEW).[46] This structure consists of four crystallographically independent Zn^{2+} ions. Two of the zinc ions are each coordinated to four bridging imidazolate linkers, bonding to another zinc atom. In contrast, the other two Zn^{2+} ions have three bridging imidazolate units and one additional imidazole that does not connect to another zinc atom and remains in its neutral form. Thus, it is remarkable that the solvent-free synthesis of the heterometallic **MUV-25(mog)** integrates zinc atoms into a topology previously elusive for this metal. This synthetic approach also overcomes the susceptibility of Fe^{2+} to oxidize to Fe^{3+} during solvothermal synthesis. In fact, we have previously employed this solvent-free synthesis method to incorporate Fe^{2+} centres into extended structures of different dimensionalities.[47,48]

For a more comprehensive understanding of the metal centres, the electronic states of Fe and Zn were analysed individually by X-ray absorption near edge spectroscopy (XANES). XANES spectra of **MUV-25(mog)** indicate exclusively octahedral Fe^{2+} ions in the network, whereas the Zn^{2+} centres have a tetrahedral geometry (see Section S5). This is consistent with the single crystal X-ray diffraction data, which provides a better refinement when the structure is modelled with the iron and zinc atoms located in the octahedral and tetrahedral environments, respectively (see Table S3†). Finally, a 1 : 2 Fe : Zn metal ratio is further confirmed with inductively coupled plasma (ICP) analysis (Table S8†). Thus, the formula of **MUV-25(mog)** is $[Fe_1Zn_2(im)_6(Him)_2]$. This structural arrangement, featuring two distinct metal coordination sites, enables the incorporation of both metal ions into the lattice in well-defined positions: zinc occupies the tetrahedral sites, while iron is confined to the octahedral sites.

Increasing the amount of iron or zinc in the synthesis leads to a mixture of compounds in which the pure iron or the pure zinc phases (**IMIDFE** and **KUMXEW**, respectively) are present together with **MUV-25(mog)**, as established by Rietveld refinement (see Fig. S7–S9†). This demonstrates that obtaining a pure phase is quite challenging, except when using a 1 : 1 starting ratio of Fe : Zn, which results in a nearly pure phase of **MUV-25(mog)** (see Fig. S1–S5†).

Upon heating **MUV-25(mog)**, thermogravimetric analysis (TGA) shows a mass loss of 19.5% around 260 °C, coinciding with an endothermic peak in the differential scanning calorimetry (DSC) measurement (Fig. 2a). This decrease in mass is likely attributed to the elimination of the terminal imidazole molecules that are bound to the octahedral iron centres, calculated to correspond to a mass loss of 18.8%, as previously noted in the pure iron phase.[36] This process is accompanied by a structural transformation, as seen in the powder X-ray diffraction (Fig. 2b). This structural rearrangement is unequivocally determined by X-ray diffraction from a single crystal obtained after heating **MUV-25(mog)** at 300 °C. The newly formed crystalline solid, of formula $[Fe_1Zn_2(im)_6]$, adopts the **zni** topology, and is therefore denoted **MUV-25(zni)**. This phase

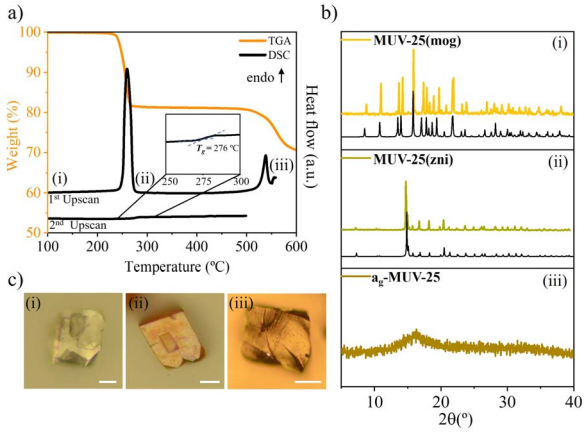

Fig. 2 (a) Thermogravimetric (in orange) and differential scanning calorimetry (in black) analyses conducted during the heating of $[Fe_1Zn_2(im)_6(Him)_2]$ (**MUV-25(mog)**), showing the mass loss and the phase transitions. (b) X-ray powder patterns of the different phases obtained upon heating at different temperatures (indicated in the DSC plot), with the calculated powder patterns as thin black lines beneath. (c) Microscope images of the different phases that correspond with (i) **MUV-25(mog)**, (ii) **MUV-25(zni)** and (iii) **a_g-MUV-25**. The scale bars correspond to 25 μm.

transition is accompanied by a slight shortening of the intermetallic distance, decreasing from 6.16 Å in **MUV-25(mog)** to 5.95 Å in **MUV-25(zni)** (Fig. 1). The structural reorganization implies a transformation of all octahedral iron centres into tetrahedral ones, while the tetrahedral zinc centres retain their configuration. This geometrical change is also confirmed by the electronic state of the Fe ions. Specifically, when examining the Fe K-edge XANES of **MUV-25(zni)**, we observe a marked increase in the pre-edge intensity with EXAFS showing a decrease in first shell coordination number, pointing to a shift to tetrahedral iron nodes (see Fig. 3d and Tables S5 and S6†).[49,50] Thus, conversion of octahedral centres to tetrahedral ones has been achieved, aligning well with the **zni** topology.

Further heating of **MUV-25(zni)** to 538 °C reveals another endothermic peak accompanied by a slight mass loss, signaling the onset of melting. This process is accompanied by minor decomposition of some imidazole ligands, likely those coordinated to iron, which may undergo oxidation during melting. Room temperature powder X-ray diffraction of the material after melt-quenching reveals the absence of Bragg reflections (Fig. 2b). This observation is supported by microscopic images showing the formation of a vitreous monolithic phase, providing initial evidence of the vitrification of **MUV-25(zni)** into a noncrystalline phase referred to as **a_g-MUV-25** (Fig. 2c and S40–S42†). This melting transition precedes material decomposition, which occurs at 550 °C.

In order to get further insights into the structural differences and similarities between the crystalline and amorphous phases of **MUV-25(mog)**, X-ray total scattering experiments were performed on **MUV-25(mog)**, **MUV-25(zni)** and **a_g-MUV-25**. The total scattering structure factors, *S(Q)*, shown in Fig. S17,† indicate that the Bragg peaks observed in the crystalline phases are absent in the **a_g-MUV-25** data. The corresponding X-ray pair

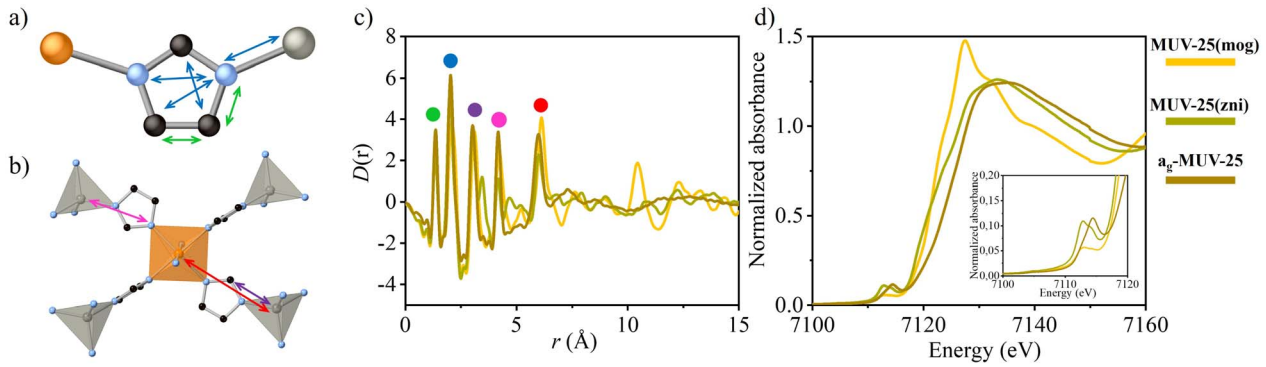

Fig. 3 (a and b) Schematic representation of the imidazolate bridge coordinated to two metals and connectivity between one octahedral iron centre to four tetrahedral zinc centres. Colour codes are the same as in Fig. 1. The coloured arrows indicate interatomic distances that match with the peaks shown in panel c. (c) X-ray PDF in the form of $D(r)$ of **MUV-25(mog)**, **MUV-25(zni)**, and **a$_g$-MUV-25**. (d) Fe K-edge rising edge spectra with inset showing the pre-edge features.

distribution function (PDF or $D(r)$) data are shown in Fig. 3. The consistency in the short-range correlations within approximately ~6 Å (corresponding to the distance between neighbouring Zn^{2+} and Fe^{2+} centres and between neighbouring Zn^{2+} and Zn^{2+} centres) across all the PDFs indicates that the tetrahedral coordination of the metal nodes with imidazolate linkers remains intact after the melting process in the **a$_g$-MUV-25**. Moreover, we can observe a small shift in the intermetallic distance (peak with red label in Fig. 3c) corresponding to the contraction of the structure after the transition from **MUV-25** to **MUV-25(zni)**, which is in agreement with the crystal structural data and the calculated PDFs (Fig. S18†). However, a peak at 3.45 Å in the PDF data from **MUV-25(zni)** does not match the calculated PDF. The calculated partial PDFs (Fig. S17–19†) did not help us identify the source of this peak. To further investigate this contribution, also observed in the PDF of **MUV-24(zni)**,[36] we calculated PDFs of various iron oxides. The PDF of spinel Fe_3O_4 exhibits similar features to these additional peaks, suggesting Fe^{3+} forms locally and indicating the reactive nature of this material (Fig. S22†). However, the peak at 3.45 Å, corresponding to iron oxide, is not observed in the PDF data from **a$_g$-MUV-25**. We hypothesize that this is due to a faster formation of iron oxide in the **zni** phase due to the instability of iron in this topology. Indeed, **MUV-24(zni)**, with 100% Fe centres, is significantly less stable, while the vitreous phase **a$_g$-MUV-24** is more stable. This higher stability against iron oxidation may be attributed to the denser packing of the amorphous phase compared to the **zni** phase, which makes the iron centres less accessible. Therefore, preventing a partial oxidation of **MUV-25(zni)** during the measurement process is more challenging compared to **a$_g$-MUV-25**. This process was further confirmed by XAS. The parent compound, **MUV-25(mog)**, exhibits a pre-edge feature at 7113.1 eV (Fig. S24 and Table S5†), attributed to 1s → 3d transitions, strongly indicating the presence of a six-coordinate (octahedral) Fe^{2+} centres, consistent with EXAFS analysis and XRD data (Fig. S25 and Table S6†). Upon heating, the formation of **MUV-25(zni)** results in a notable increase in pre-edge intensity, consistent with tetrahedral Fe^{2+} centres. In addition, the observed shift towards higher energy values (~1 eV) suggests partial oxidation to Fe^{3+}. This demonstrates the coexistence of Fe^{2+} and Fe^{3+} in **MUV-25(zni)**, with their relative amounts depending on the duration of air exposure.

Further heating results in **a$_g$-MUV-25**, where the XANES spectra at the Fe K-edge is consistent with a tetrahedral geometry, although a ~1 eV shift to higher energy in the pre-edge suggests partial oxidation which was not observed in the PDF analysis. Furthermore, EXAFS analysis shows weaker intensities in the longer-range structure (2–4 Å) consistent with a less ordered system. Lastly, EXAFS also suggests the formation of minor amounts of Fe oxides. Interestingly, EXAFS at the Zn K-edge shows spectra with a similar profile in all the cases (Fig. S23†) and only minor differences in the XANES region previously attributed to different binding modes of the imidazole (Him) ligands,[50,51] suggesting that the Fe centres are predominantly responsible for the morphological changes observed.

Significant differences emerge when comparing the phase transformations of the heterometallic **MUV-25** with its pure homometallic counterparts, **IMIDFE** (iron-based) and **KUMXEW** (zinc-based) (Fig. 4), both prepared *via* solvent-free synthesis. Initially, **MUV-25** adopts the same **mog** topology as **IMIDFE**, whereas **KUMXEW** exhibits the distinct **moc** topology, in which no octahedral centres are present. In all these initial phases, neutral imidazoles are coordinated to some of the metal centres, and the first phase transition is consistently associated with the decoordination of these neutral imidazoles. This process is evidenced by a drop in the TGA curve accompanying an endothermal peak (between 200 and 350 °C), leading to the formation of the thermodynamically stable **zni** phase in the **MUV-25** and **KUMXEW**. However, for **IMIDFE**, an additional phase transition occurs prior to reaching the **zni** phase, resulting in the intermediate **lla** phase. The TGA drop associated with the decoordination of neutral imidazoles corresponds to calculated values of 19.3% for **IMIDFE**, 18.8% for **MUV-25**, and 7.9% for **KUMXEW**, which is in good agreement with the experimental data (21.3%, 19.5% in and 7.9%, respectively, see Fig. 4a).

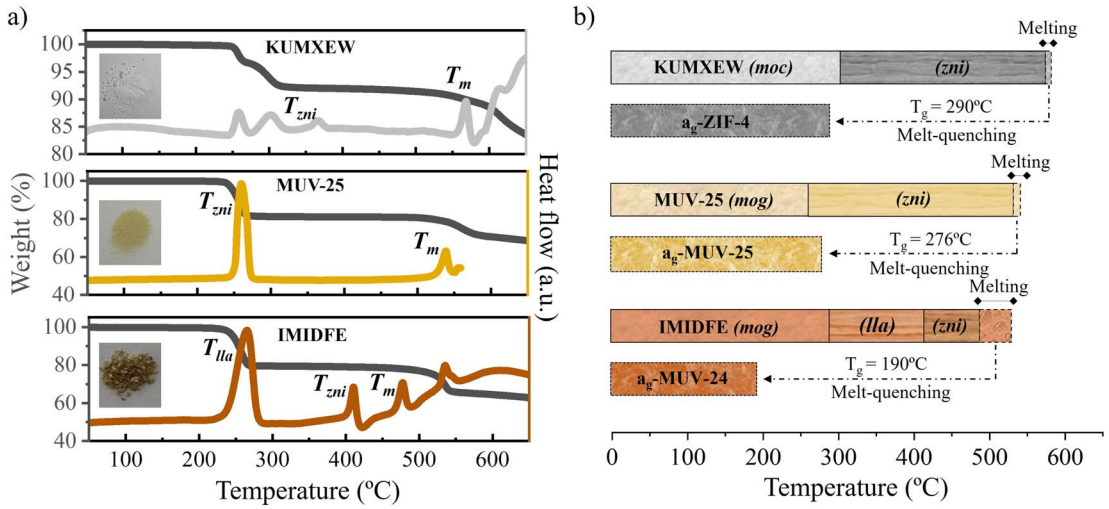

Fig. 4 (a) TGA (dark grey lines, left vertical scale) and DSC (grey, yellow and brown lines, right vertical scale) traces of **KUMXEW** (Zn), **MUV-25** (Fe/Zn) and **IMIDFE** (Fe), along with their corresponding optical images. The samples were heated at 10 °C min^{-1}. (b) Schematic representation of the different phase transition undergone by **KUMXEW**, **MUV-25** and **IMIDFE**.

Interestingly, the heterometallic **MUV-25** transitions directly to the **MUV-25(zni)** phase at a significantly lower temperature (260 °C) compared to the pure homometallic materials, a phase that appears upon heating at 417 °C (**IMIDFE**) and 360 °C (**KUMXEW**). We hypothesize that in the case of **IMIDFE**, the high transition temperature to the zni phase is due to the formation of a stable intermediate phase, known as **MUV-25(lla)**, immediately after the decoordination of the neutral imidazoles. In contrast, in the case of **KUMXEW**, the removal of the neutral imidazoles implies the rupture of Zn–N bonds which are stronger than Fe–N bonds.[47] This stronger bonding delays the phase transition associated with the removal of the linkers.

Upon further heating, an additional endothermic peak appears, corresponding to the melting of the compounds. For both **KUMXEW** and **MUV-25**, this melting is accompanied by a slight mass loss. A similar problem has been previously observed in other materials that melt at high temperatures, such as **ZIF-4**,[28] although the isolation of the vitreous phase is still possible in these cases. Analysis of the melting temperature, T_m, of the three materials, **MUV-25**, **IMIDFE** and **KUMXEW**, shows that T_m increases with the Zn content in the framework, *i.e.* T_m(IMIDFE) < T_m(MUV-25) < T_m(KUMXEW). This trend aligns with the physical expectations, as the melting process involves dynamic dissociation and reassociation of metal-linker bonds, with Zn–N bonds being more stable than Fe–N bonds.[47] Interestingly, despite the presence of two distinct bonding energies in **MUV-25**, the DSC analysis shows only a single melting feature, indicating a high degree of cooperativity and homogeneity in the M–N bonds within the lattice.

The enthalpy of melting (ΔH_m), determined by integrating the DSC melting peak, was calculated for three compounds (Fig. S30–S32†). For **KUMXEW**, the experimental ΔH_m value is 12.1 kJ mol^{-1}, which is comparable to the reported values for **ZIF-4** (11.5 kJ mol^{-1}) and **ZIF-zni** (11.9 kJ mol^{-1}).[8b] However, introducing iron into the lattice leads to a decrease in ΔH_m, with values of 8.5 kJ mol^{-1} for **MUV-25** and 6.6 kJ mol^{-1} for **IMIDFE**. In this case, we assume that the packing density before and after melting remains similar, so the decrease in ΔH_m cannot be attributed to a less tightly packed lattice with lower lattice energy, as observed in **ZIF-62**. Instead, as with T_m, we attribute this decrease in ΔH_m to the stronger Zn–N bonds, which create a more stable crystalline framework. This stability requires higher energy values to overcome during the transition from the solid to the liquid state, resulting in a higher ΔH_m. In contrast, the weaker Fe–N bonds lead to a less stable framework, lowering the energy required for melting and thus reducing ΔH_m.

After studying all the different transformations that the material undergoes during the initial upscan, we conducted a cyclic upscan under a N_2 atmosphere from room temperature to 550 °C at a rate of 10 °C min^{-1} (see Fig. S33†) to determine the glass transition temperature (T_g). During the first upscan, the material undergoes all the transformations described earlier. Subsequently, a downscan was performed to obtain the melt-quenched glass, and during a second upscan of **a_g-MUV-25**, a calorimetric signal associated with the glass transition temperature (T_g) was observed at 276 °C. This temperature is quite similar to that of **a_g-KUMXEW** (290 °C), but significantly different from that of **a_g-MUV-24** (190 °C) (Fig. S34†).

To further analyze the glassy features of **MUV-25**, the liquid fragility has been examined. The liquid fragility index (m) is used to describe the sensitivity of a material to physical aging, and it can be calculated using different approaches: (i) through viscosity experiments across T_g using the Angell plot and the MYEGA viscosity model or (ii) by DSC using the Arrhenius equation (eqn (1)), where the liquid fragility parameter (m) can be defined as:

$$m = -\left(\frac{\mathrm{d}\log\ \beta_c}{\mathrm{d}\left(T_{f,ref}/T_f\right)}\right) \quad (1)$$

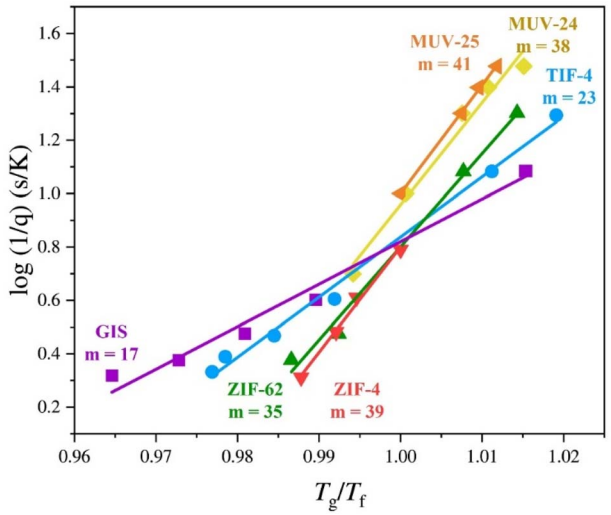

Fig. 5 Fragilities of a_g-ZIF-4, a_g-Zn(im)$_2$ (GIS), a_g-TIF-4, a_g-ZIF-62, a_g-MUV-24 and a_g-MUV-25 determined from the dependence of fictive temperature (T_f) on the heating rate (q_h) by using the DSC method.

where β_c is the cooling rate, T_f is the fictive temperature measured on heating and $T_{f,ref}$ is the reference fictive temperature or T_g. T_f is defined as the extrapolated intersection of the pre-transition and post-transition DSC baselines in enthalpy units. To obtain enthalpy, DSC heat flow curves are integrated. The unique property of the fictive temperature is dependent of the DSC heating rate used to measure it. Hence, T_f shift to higher temperature values using increasing heating rates.

DSC curves at different heating ratios were recorded for **a_g-MUV-24** and **a_g-MUV-25** (Fig. S35†). Liquid fragility (m) was calculated using eqn (1) (Fig. S36 and Table S9†) with values of 41 and 38 for **a_g-MUV-25** and **a_g-MUV-24**, respectively, very similar to the reported value for **a_g-ZIF-4** (ref. 28) (Fig. 5). This suggests that m is largely independent of the presence of Fe or Zn.

Conclusions

We have successfully synthesized a novel glass forming heterometallic material, **MUV-25(mog)**, *via* solvent-free synthesis. This compound, consisting of iron and zinc centres, serves as a platform for preparing the thermally activated **zni** topology, that melts at an intermediate temperature between the pure counterparts. This **mog** topology has a structure in which the metal centres occupy different positions, the Fe^{2+} are in octahedral sites, while the Zn^{2+} ions are tetrahedrally coordinated. After a first heating process a rearrangement of the network takes place and all the iron centres transition from octahedral to tetrahedral, while the zinc centres maintain their tetrahedral environment, yielding the **zni** topology. The arrangement of each metal site has been precisely followed by spectroscopic techniques. The incorporation of two different metal nodes enables the **zni** phase to be obtained through a temperature phase transition at ambient pressure at lower temperatures than previously reported. Ultimately, a molten state is achieved yielding a heterometallic glass with liquid fragility properties similar to the pure counterparts. With this work, we aim to highlight the significant impact of introducing different metals into the same lattice, not only from a crystallographic perspective but also in terms of thermal properties. The inclusion of a second metal could also serve as a powerful tool for developing multifunctional glasses, just as it has proven to be in crystalline MOFs for tuning gas separation, luminescence, and sensing properties.

Experimental methods

Synthesis of MUV-25

A mixture of ferrocene (14 mg, 0.07 mmol), ZnO (6 mg, 0.07 mmol) and imidazole (20 mg, 0.3 mmol) were combined and sealed under vacuum in a layering tube (4 mm diameter). The mixture was heated at 150 °C for 24 hours. The product was allowed to cool to room temperature, and the layering tube was then opened. The unreacted precursors were extracted with acetonitrile. **MUV-25(mog)** was isolated as yellow crystals. Phase purity was established by X-ray powder diffraction.

Synthesis of MUV-25(zni)

Approximately 15 mg of **MUV-25(mog)** were treated with the following thermal process: $T_{initial}$ = 40 °C (15 min) → 300 °C → 25 °C. Heating and cooling rates = 10 °C min^{-1}. Once the process is completed, phase **MUV-25(zni)** is isolated. Phase purity was established by X-ray powder diffraction.

Synthesis of a_g-MUV-25

Approximately 15 mg of **MUV-25(mog)** were treated with the following thermal process: $T_{initial}$ = 40 °C (15 min) → 550 °C (10 min) → 25 °C. Heating and cooling rates = 10 °C min^{-1}. Once the process is completed, phase **a_g-MUV-25** is isolated. The absence of crystalline phases was established by X-ray powder diffraction.

MUV-25(mog), **MUV-25(zni)** and **a_g-MUV-25** were further characterized using PXRD, TGA, ICP-MS, SEM-EDS, NMR, FTIR, and polarized light microscopy. More detailed information can be found in the ESI.†

Synthesis of KUMXEW

A mixture of ZnO (12 mg, 0.14 mmol) and imidazole (20 mg, 0.3 mmol) were combined and sealed under vacuum in a layering tube (4 mm diameter). The mixture was heated at 150 °C for 24 hours. The product was allowed to cool to room temperature, and the layering tube was then opened. The unreacted precursors were extracted with acetonitrile. **KUMXEW** was isolated as white crystals. Phase purity was established by X-ray powder diffraction.

Synthesis of IMIDFE

A mixture of ferrocene (28 mg, 0.14 mmol) and imidazole (20 mg, 0.3 mmol) were combined and sealed under vacuum in a layering tube (4 mm diameter). The mixture was heated at 150 °C for 96 hours. The product was allowed to cool to room

temperature, and the layering tube was then opened. The unreacted precursors were extracted with acetonitrile. **IMIDFE** was isolated as orange crystals. Phase purity was established by X-ray powder diffraction.

Single-crystal diffraction

Single crystals of **MUV-25(mog)** and **MUV-25(zni)** were mounted on glass fibers using a viscous hydrocarbon oil to coat the crystals and then transferred directly to the cold nitrogen stream for data collection. X-ray data were collected at 120 K on a DW rotating anode Rigaku Synergy-R diffractometer with (Cu-K_α) X-ray source ($\lambda = 1.54184$ Å). Data were measured using the CrysAlisPro suite of programs. The program CrysAlisPro, Rigaku, was used for unit cell determinations and data reduction. Empirical absorption correction was performed using spherical harmonics, implemented in the SCALE3 ABSPACK scaling algorithm, based upon symmetry-equivalent reflections combined with measurements at different azimuthal angles. The crystal structures were solved and refined against all F^2 values using the SHELXL and Olex2 suite of programs.[52,53] Atomic displacement parameters of all non-hydrogen atoms were refined anisotropically except those within a disordered imidazolate ring in each structure, which were refined isotropically. Hydrogen atoms were placed in calculated positions, refined using idealized geometries (riding model) and assigned fixed isotropic atomic displacement parameters. CCDC 2373266–2373267 contain the supplementary crystallographic data for this paper.

Differential scanning calorimetry (DSC)

Differential scanning calorimetry (DSC) measurements were conducted on a TRIOS DSC 250 instrument. 10–15 mg of activated sample was loaded into an aluminium crucible (30 μL) with a pierced lid. An empty aluminium crucible was used as a reference. Under N_2 gas, the sample was heated to a temperature of 40 °C and an isotherm was performed for 15 min to stabilize the sample. Then the sample was heated to 300 °C, and 550 °C at a rate of 10 °C min^{-1} for **MUV-25(zni)**, and **a_g-MUV-25**, respectively. Upon reaching the temperature, an isotherm of 10 min was performed to ensure a complete phase change. This was followed by cooling back to 40 °C at 10 °C min^{-1}. Using a NETSCH DSC 214 Polyma instrument, we measured the fictive temperature based on varying up- and downscan rates. By analyzing the dependence of the fictive temperature on the heating rate, we calculated the liquid fragility indices following established methods in the literature.[28] Approximately 5–10 mg of powdered samples were placed in sealed 70 μL aluminum crucibles with a hole punctured in the lid to prevent pressure build-up. An empty aluminum pan was used as a reference. Background corrections were performed using the same heating cycle on an empty aluminum crucible. All data analysis was performed using the Netzsch Proteus software package.

X-ray total scattering

MUV-25(mog), **MUV-25(zni)** and **a_g-MUV-25** data were collected at beamline I15-1, Diamond Light Source, UK (EE200338). All powdered samples were ground and loaded into kapton® capillaries (1 mm diameter) to a height of 0.5 cm. The capillaries were sealed with plasticine either side of the sample and placed over an inner stainless steel rod before being mounted onto the beamline. Total scattering data were collected at room temperature for the background (*i.e.*, empty instrument), empty kapton capillary, and for all samples in a Q range of 0.2–26.0 $Å^{-1}$ ($\lambda = 0.161669$ Å, 76.69 keV). Subsequent Fourier transformations of the processed total scattering data resulted in a real-space PDF $G(r)$ for each material. In this work, we use the $D(r)$ form of the PDF to accentuate high r correlations. All processing of the total scattering data was performed using GudRunX following well-documented procedures.[54,55]

X-ray absorption spectroscopy (XAS)

Samples were run as solid powders diluted in cellulose at the ALBA synchrotron CLAESS beamline. Data was collected in transmission mode, at liquid nitrogen temperatures (80 K), using a Si(111) double crystal monochromator. Data was averaged, normalized and calibrated using the Athena software.[56] The energy was calibrated to the first inflection point of Fe foil (7112 eV) and Zn foil (9659 eV) for Fe and Zn K-edge data, respectively. The autobk algorithm was used for EXAFS spectra extraction as described in the ESI Section 5.† The FEFF6 code[56,57] was used for scattering path generation, and $k^{1,2,3}$-weighted fits of the data were carried out in r-space, over r-ranges and k-ranges as specified, in ESI Section 5† using the python implementation of the Artemis software (Larch).[58] A fixed global $S_0{}^2$ value and floating E_0 were employed with the initial E_0 value set to the inflection point of the rising edge. Single scattering paths were fit in terms of a Δr_{eff} and σ^2 as previously described. To assess the goodness of the fits both the R_{factor} (%R) and the reduced χ^2 ($\chi_\nu{}^2$) were minimized, ensuring that the data was not over-fit. Pre-edge features were fit using a Gaussian–Lorentzian sum function with 50% Gaussian character.

Data availability

The data supporting this article have been included as part of the ESI. The characterization data files are available on Zenodo open repository (DOI: 10.5281/zenodo.15113164).†

Author contributions

L. L. A. synthesized and characterized the materials. C. C. B. and T. D. B. conducted the liquid fragility experiments. L. L. A. performed the X-ray total scattering experiments and analysis under the supervision of C. C. B. and D. A. K. C. C. B performed the partial PDF analysis. I. S. carried out the Rietveld refinements. V. M. D. performed the XAS measurements and analyzed the data. G. M. E. conceived the idea and designed the experiments. L. L. A. and G. M. E. prepared the manuscript, with all authors contributing to its preparation.

Conflicts of interest

The authors declare no competing finantial interests.

Acknowledgements

This work has been supported by the European Union (ERC-2016-CoG 724681 S-CAGE), grants PID2023-152920NB-I00, and María de Maeztu Centre of Excellence Programe CEX2019-000919 M, funded by MCIN/AEI/10.13039/501100011033 and cofinanced by FEDER, and the Generalitat Valenciana (CIPROM/2022/48, and IDIFEDER2021/075). L. L.-A. thanks MICIN for a pre-doctoral fellowship (PRE2019-089295). This study forms part of the Advanced Materials program and was supported by MCIN with funding from European Union Next-GenerationEU (PRTR-C17.I1) and by Generalitat Valenciana (projects MFA/2022/31). We also thank the University of Valencia for research facilities (SCSIE). C. C.-B. and T. D. B. acknowledge the Leverhulme Trust for a Research Project Grant (RPG-2020-005). X-ray absorption experiments were performed at the CLAESS beamline at ALBA Synchrotron with the collaboration of ALBA staff (V. M.-D.) as part of experiments 2022035791 and 2024017988. We thank M. Vicent-Morales and I. Abanades-Lazaro for assistance in the preliminary EXAFS experiments. We extend our gratitude to Diamond Light Source, Rutherford Appleton Laboratory, U.K., for the synchrotron access to Beamline I15-1 (CY29957) and Philip A. Chater for their assistance. T. D. B. would like to thank the Royal Society for a University Research Fellowship and Research Grant (URF\R\211013 and RGS\R2\212221).

Notes and references

1 (*a*) N. Ma and S. Horike, Metal–Organic Network-Forming Glasses, *Chem. Rev.*, 2022, **122**, 4163–4203; (*b*) N. Ma, S. Kosasang, E. K. Berdichevsky, T. Nishiguchi and S. Horike, Functional metal–organic liquids, *Chem. Sci.*, 2024, **15**, 7474–7501.

2 T. D. Bennett and S. Horike, Liquid, Glass and Amorphous Solid States of Coordination Polymers and Metal–Organic Frameworks, *Nat. Rev. Mater.*, 2018, **3**, 431–440.

3 S. Horike, S. S. Nagarkar, T. Ogawa and S. Kitagawa, A New Dimension for Coordination Polymers and Metal–Organic Frameworks: Towards Functional Glasses and Liquids, *Angew. Chem., Int. Ed.*, 2020, **59**, 6652–6664.

4 H. Tao, T. D. Bennett and Y. Yue, Melt-Quenched Hybrid Glasses from Metal–Organic Frameworks, *Adv. Mater.*, 2017, **29**, 1601705.

5 J. Hou, A. F. Sapnik and T. D. Bennett, Metal-Organic Framework Gels and Monoliths, *Chem. Sci.*, 2020, **11**, 310–323.

6 N. Ma, S. Impeng, S. Bureekaew, N. Morozumi, M. A. Haga and S. Horike, Photoexcited Anhydrous Proton Conductivity in Coordination Polymer Glass, *J. Am. Chem. Soc.*, 2023, **145**, 9808–9814.

7 S. S. Sørensen, M. B. Østergaard, M. Stepniewska, H. Johra, Y. Yue and M. M. Smedskjaer, Metal-Organic Framework Glasses Possess Higher Thermal Conductivity than Their Crystalline Counterparts, *ACS Appl. Mater. Interfaces*, 2020, **12**, 18893–18903.

8 (*a*) O. Smirnova, S. Hwang, R. Sajzew, L. Ge, A. Reupert, V. Nozari, S. Savani, C. Chmelik, M. R. Reithofer, L. Wondraczek, J. Kärger and A. Knebel, Precise Control over Gas-Transporting Channels in Zeolitic Imidazolate Framework Glasses, *Nat. Mater.*, 2023, **23**, 262–270; (*b*) L. Frentzel-Beyme, P. Kolodzeiski, J. B. Weiß, A. Schneemann and S. Henke, Quantification of Gas-Accessible Microporosity in Metal-Organic Framework Glasses, *Nat. Commun.*, 2022, **13**, 7750.

9 (*a*) T. To, S. S. Sørensen, M. Stepniewska, A. Qiao, L. R. Jensen, M. Bauchy, Y. Yue and M. M. Smedskjaer, Fracture Toughness of a Metal–Organic Framework Glass, *Nat. Commun.*, 2020, **11**, 2593; (*b*) S. Li, R. Limbach, L. Longley, A. A. Shirzadi, J. C. Walmsley, D. N. Johnstone, P. A. Midgley, L. Wondraczek and T. D. Bennett, Mechanical Properties and Processing Techniques of Bulk Metal−Organic Framework Glasses, *J. Am. Chem. Soc.*, 2019, **141**, 1027–1034.

10 S. Horike, N. Ma, Z. Fan, S. Kosasang and M. M. Smedskjaer, Mechanics, Ionics, and Optics of Metal-Organic Framework and Coordination Polymer Glasses, *Nano Lett.*, 2021, **21**, 6382–6390.

11 M. Liu, A. H. Slavney, S. Tao, R. D. McGillicuddy, C. C. Lee, M. B. Wenny, S. J. L. Billinge and J. A. Mason, Designing Glass and Crystalline Phases of Metal-Bis(Acetamide) Networks to Promote High Optical Contrast, *J. Am. Chem. Soc.*, 2022, **144**, 22262–22271.

12 Y. Zhao, S. Y. Lee, N. Becknell, O. M. Yaghi and C. A. Angell, Nanoporous Transparent MOF Glasses with Accessible Internal Surface, *J. Am. Chem. Soc.*, 2016, **138**, 10818–10821.

13 J. Fonseca, T. Gong, L. Jiao and H.-L. Jiang, Metal-Organic Frameworks (MOFs) beyond Crystallinity: Amorphous MOFs, MOF Liquids and MOF Glasses, *J. Mater. Chem. A*, 2021, **9**, 10562–10611.

14 Y. Song, Y. Ren, H. Cheng, Y. Jiao, S. Shi, L. Gao, H. Xie, J. Gao, L. Sun and J. Hou, Metal-Organic Framework Glass Catalysts from Melting Glass-Forming Cobalt-Based Zeolitic Imidazolate Framework for Boosting Photoelectrochemical Water Oxidation, *Angew. Chem., Int. Ed.*, 2023, **62**, e202306420.

15 R. Lin, X. Li, A. Krajnc, Z. Li, M. Li, W. Wang, L. Zhuang, S. Smart, Z. Zhu, D. Appadoo, J. R. Harmer, Z. Wang, A. G. Buzanich, S. Beyer, L. Wang, G. Mali, T. D. Bennett, V. Chen and J. Hou, Mechanochemically Synthesised Flexible Electrodes Based on Bimetallic Metal–Organic Framework Glasses for the Oxygen Evolution Reaction, *Angew. Chem., Int. Ed.*, 2022, **61**, e202112880.

16 J. Hou, P. Chen, A. Shukla, A. Krajnc, T. Wang, X. Li, R. Doasa, L. H. G. Tizei, B. Chan, D. N. Johnstone, R. Lin, T. U. Schülli, I. Martens, D. Appadoo, M. S. Ari, Z. Wang, T. Wei, S. C. Lo, M. Lu, S. Li, E. B. Namdas, G. Mali, A. K. Cheetham, S. M. Collins, V. Chen, L. Wang and T. D. Bennett, Liquid-Phase Sintering of Lead Halide

Perovskites and Metal-Organic Framework Glasses, *Science*, 2021, **374**, 621–625.

17 Y. Wang, H. Jin, Q. Ma, K. Mo, H. Mao, A. Feldhoff, X. Cao, Y. Li, F. Pan and Z. Jiang, A MOF Glass Membrane for Gas Separation, *Angew. Chem., Int. Ed.*, 2020, **59**, 4365–4369.

18 D. Ao, Z. Yang, Z. Qiao, Y. Sun, Z. Zhang, M. D. Guiver and C. Zhong, Metal–Organic Framework Crystal–Glass Composite Membranes with Preferential Permeation of Ethane, *Angew. Chem., Int. Ed.*, 2023, **62**, e202304535.

19 J. Hou, C. W. Ashling, S. M. Collins, A. Krajnc, C. Zhou, L. Longley, D. N. Johnstone, P. A. Chater, S. Li, M. V. Coulet, P. L. Llewellyn, F. X. Coudert, D. A. Keen, P. A. Midgley, G. Mali, V. Chen and T. D. Bennett, Metal-Organic Framework Crystal-Glass Composites, *Nat. Commun.*, 2019, **10**, 2580.

20 C. Gao, Z. Jiang, S. Qi, P. Wang, L. R. Jensen, M. Johansen, C. K. Christensen, Y. Zhang, D. B. Ravnsbæk and Y. Yue, Metal-Organic Framework Glass Anode with an Exceptional Cycling-Induced Capacity Enhancement for Lithium-Ion Batteries, *Adv. Mater.*, 2022, **34**, 2110048.

21 R. Gaillac, P. Pullumbi, K. A. Beyer, K. Chapman, D. A. Keen, T. D. Bennett and F. X. Coudert, Liquid Metal–Organic Frameworks, *Nat. Mater.*, 2017, **16**, 1149–1154.

22 M. Dinca and J. R. Long, Introduction: Porous Framework Chemistry, *Chem. Rev.*, 2020, **120**, 8037–8038.

23 M. Kim, H. S. Lee, D. H. Seo, S. J. Cho, E. C. Jeon and H. R. Moon, Melt-Quenched Carboxylate Metal–Organic Framework Glasses, *Nat. Commun.*, 2024, **15**, 1174.

24 M. Liu, R. D. McGillicuddy, H. Vuong, S. Tao, A. H. Slavney, M. I. Gonzalez, S. J. L. Billinge and J. A. Mason, Network-Forming Liquids from Metal-Bis(Acetamide) Frameworks with Low Melting Temperatures, *J. Am. Chem. Soc.*, 2021, **143**, 2801–2811.

25 W. L. Xue, G. Q. Li, H. Chen, Y. C. Han, L. Feng, L. Wang, X. L. Gu, S. Y. Hu, Y. H. Deng, L. Tan, M. T. Dove, W. Li, J. Zhang, H. Dong, Z. Chen, W. H. Deng, G. Xu, G. Wang and C. Q. Wan, Melt-Quenched Glass Formation of a Family of Metal-Carboxylate Frameworks, *Nat. Commun.*, 2024, **15**, 2040.

26 W. L. Xue, P. Kolodzeiski, H. Aucharova, S. Vasa, A. Koutsianos, R. Pallach, J. Song, L. Frentzel-Beyme, R. Linser and S. Henke, Highly Porous Metal-Organic Framework Liquids and Glasses via a Solvent-Assisted Linker Exchange Strategy of ZIF-8, *Nat. Commun.*, 2024, **15**, 4420.

27 J. Song, L. Frentzel-Beyme, R. Pallach, P. Kolodzeiski, A. Koutsianos, W. L. Xue, R. Schmid and S. Henke, Modulating Liquid-Liquid Transitions and Glass Formation in Zeolitic Imidazolate Frameworks by Decoration with Electron-Withdrawing Cyano Groups, *J. Am. Chem. Soc.*, 2023, **145**, 9273–9284.

28 T. D. Bennett, J. C. Tan, Y. Yue, E. Baxter, C. Ducati, N. J. Terrill, H. H. M. Yeung, Z. Zhou, W. Chen, S. Henke, A. K. Cheetham and G. N. Greaves, Hybrid Glasses from Strong and Fragile Metal-Organic Framework Liquids, *Nat. Commun.*, 2015, **6**, 8079.

29 K. S. Park, Z. Ni, A. P. Côté, J. Y. Choi, R. Huang, F. J. Uribe-Romo, H. K. Chae, M. O'Keeffe and O. M. Yaghi, Exceptional Chemical and Thermal Stability of Zeolitic Imidazolate Frameworks, *Proc. Natl. Acad. Sci. U. S. A.*, 2006, **103**, 10186–10191.

30 L. Frentzel-Beyme, M. Kloß, P. Kolodzeiski, R. Pallach and S. Henke, Meltable Mixed-Linker Zeolitic Imidazolate Frameworks and Their Microporous Glasses: From Melting Point Engineering to Selective Hydrocarbon Sorption, *J. Am. Chem. Soc.*, 2019, **141**, 12362–12371.

31 T. D. Bennett, Y. Yue, P. Li, A. Qiao, H. Tao, N. G. Greaves, T. Richards, G. I. Lampronti, S. A. T. Redfern, F. Blanc, O. K. Farha, J. T. Hupp, A. K. Cheetham and D. A. Keen, Melt-Quenched Glasses of Metal-Organic Frameworks, *J. Am. Chem. Soc.*, 2016, **138**, 3484–3492.

32 C. Healy, K. M. Patil, B. H. Wilson, L. Hermanspahn, N. C. Harvey-Reid, B. I. Howard, C. Kleinjan, J. Kolien, F. Payet, S. G. Telfer, P. E. Kruger and T. D. Bennett, The Thermal Stability of Metal-Organic Frameworks, *Coord. Chem. Rev.*, 2020, **419**, 213388.

33 J. Hou, M. L. Ríos Gómez, A. Krajnc, A. McCaul, S. Li, A. M. Bumstead, A. F. Sapnik, Z. Deng, R. Lin, P. A. Chater, D. S. Keeble, D. A. Keen, D. Appadoo, B. Chan, V. Chen, G. Mali and T. D. Bennett, Halogenated Metal-Organic Framework Glasses and Liquids, *J. Am. Chem. Soc.*, 2020, **142**, 3880–3890.

34 C. Zhou, L. Longley, A. Krajnc, G. J. Smales, A. Qiao, I. Erucar, C. M. Doherty, A. W. Thornton, A. J. Hill, C. W. Ashling, O. T. Qazvini, S. J. Lee, P. A. Chater, N. J. Terrill, A. J. Smith, Y. Yue, G. Mali, D. A. Keen, S. G. Telfer and T. D. Bennett, Metal-Organic Framework Glasses with Permanent Accessible Porosity, *Nat. Commun.*, 2018, **9**, 5042.

35 L. Frentzel-Beyme, M. Kloß, R. Pallach, S. Salamon, H. Moldenhauer, J. Landers, H. Wende, J. Debus and S. Henke, Porous Purple Glass – a Cobalt Imidazolate Glass with Accessible Porosity from a Meltable Cobalt Imidazolate Framework, *J. Mater. Chem. A*, 2019, **7**, 985–990.

36 L. León-Alcaide, R. S. Christensen, D. A. Keen, J. L. Jordá, I. Brotons-Alcázar, A. Forment-Aliaga and G. Mínguez Espallargas, Meltable, Glass-Forming, Iron Zeolitic Imidazolate Frameworks, *J. Am. Chem. Soc.*, 2023, **145**, 11258–11264.

37 S. Abednatanzi, P. Gohari Derakhshandeh, H. Depauw, F. X. Coudert, H. Vrielinck, P. Van Der Voort and K. Leus, Mixed-Metal Metal–Organic Frameworks, *Chem. Soc. Rev.*, 2019, **48**, 2535–2565.

38 (*a*) M. A. Ali, X. Liu, Y. Li, J. Ren and J. Qiu, Nonlinear-Optical Response in Zeolitic Imidazolate Framework Glass, *Inorg. Chem.*, 2020, **59**, 8380–8386; (*b*) M. F. Thorne, M. L. R. Gómez, A. M. Bumstead, S. Li and T. D. Bennett, Mechanochemical Synthesis of Mixed Metal, Mixed Linker, Glass-Forming Metal-Organic Frameworks, *Green Chem.*, 2020, **22**, 2505–2512.

39 L. Longley, S. M. Collins, C. Zhou, G. J. Smales, S. E. Norman, N. J. Brownbill, C. W. Ashling, P. A. Chater, R. Tovey, C. B. Schönlieb, T. F. Headen, N. J. Terrill, Y. Yue,

A. J. Smith, F. Blanc, D. A. Keen, P. A. Midgley and T. D. Bennett, Liquid Phase Blending of Metal-Organic Frameworks, *Nat. Commun.*, 2018, **9**, 2135.

40 (*a*) M. A. Ali, J. Ren, T. Zhao, X. Liu, Y. Hua, Y. Yue and J. Qiu, Broad Mid-Infrared Luminescence in a Metal-Organic Framework Glass, *ACS Omega*, 2019, **4**, 12081–12087; (*b*) R. S. K. Madsen, M. Stepniewska, Y. Yang, A. Qiao, W. M. W. Winters, C. Zhou, J. K. Onig, J. C. Mauro and Y. Yue, Mixed Metal Node Effect in Zeolitic Imidazolate Frameworks, *RSC Adv.*, 2022, **12**, 10815–10824.

41 J. Zhang, L. Longley, H. Liu, C. W. Ashling, P. A. Chater, K. A. Beyer, K. W. Chapman, H. Tao, D. A. Keen, T. D. Bennett and Y. Yue, Structural Evolution in a Melt-Quenched Zeolitic Imidazolate Framework Glass during Heat-Treatment, *Chem. Commun.*, 2019, **55**, 2521–2524.

42 K. Noh, J. Lee and J. Kim, Compositions and Structures of Zeolitic Imidazolate Frameworks, *Isr. J. Chem.*, 2018, **58**, 1075–1088.

43 C. Castillo-Blas, A. M. Chester, D. A. Keen and T. D. Bennett, Thermally Activated Structural Phase Transitions and Processes in Metal-Organic Frameworks, *Chem. Soc. Rev.*, 2024, **53**, 3606–3629.

44 S. J. Rettig, A. Storr, D. A. Summers, R. C. Thompson and J. Trotter, Transition Metal Azolates from Metallocenes. 2. Synthesis, X-Ray Structure, and Magnetic Properties of a Three-Dimensional Polymetallic Iron(II) Imidazolate Complex, a Low-Temperature Weak Ferromagnet, *J. Am. Chem. Soc.*, 1997, **119**, 8675–8680.

45 K. Müller-Buschbaum and F. Schönfeld, The Utilisation of Solvent-Free Synthesis for the Reaction of Cobalt with Imidazole: MOF Conversion from $[Co_3(Im)_6(ImH)_2]$ via $[Co_4(Im)_8(ImH)]$ to $[Co(Im)_2]$, *Z. Anorg. Allg. Chem.*, 2011, **637**, 955–960.

46 G. A. V. Martins, P. J. Byrne, P. Allan, S. J. Teat, A. M. Z. Slawin, Y. Li and R. E. Morris, The Use of Ionic Liquids in the Synthesis of Zinc Imidazolate Frameworks, *Dalton Trans.*, 2010, **39**, 1758–1762.

47 L. León-Alcaide, J. López-Cabrelles, M. Esteve-Rochina, E. Ortí, J. Calbo, B. A. H. Huisman, M. Sessolo, J. C. Waerenborgh, B. J. C. Vieira and G. Mínguez Espallargas, Implementing Mesoporosity in Zeolitic Imidazolate Frameworks through Clip-Off Chemistry in Heterometallic Iron-Zinc ZIF-8, *J. Am. Chem. Soc.*, 2023, **145**, 23249–23256.

48 J. López-Cabrelles, J. Romero, G. Abellán, M. Giménez-Marqués, M. Palomino, S. Valencia, F. Rey and G. Mínguez Espallargas, Solvent-Free Synthesis of ZIFs: A Route toward the Elusive Fe(II) Analogue of ZIF-8, *J. Am. Chem. Soc.*, 2019, **141**, 7173–7180.

49 P. Chandrasekaran, S. C. E. Stieber, T. J. Collins, L. Que, F. Neese and S. Debeer, Prediction of High-Valent Iron K-Edge Absorption Spectra by Time-Dependent Density Functional Theory, *Dalton Trans.*, 2011, **40**, 11070–11079.

50 T. E. Westre, P. Kennepohl, J. G. DeWitt, B. Hedman, K. O. Hodgson and E. I. Solomon, A Multiplet Analysis of Fe K-Edge 1s → 3d Pre-Edge Features of Iron Complexes, *J. Am. Chem. Soc.*, 1997, **119**, 6297–6314.

51 R. Boada, J. Chaboy, S. Hayama, L. L. Keenan, A. A. Freeman, M. Amboage and S. Diáz-Moreno, Unraveling the Molecular Details of the "Gate Opening" Phenomenon in ZIF-8 with X-Ray Absorption Spectroscopy, *J. Phys. Chem. C*, 2022, **126**, 5935–5943.

52 G. M. Sheldrick, SHELXT – Integrated space-group and crystal-structure determination, *Acta Crystallogr.*, 2015, **71**, 3–8.

53 O. V. Dolomanov, L. J. Bourhis, R. J. Gildea, J. A. K. Howard and H. Puschmann, OLEX2: A Complete Structure Solution, Refinement and Analysis Program, *J. Appl. Crystallogr.*, 2009, **42**, 339–341.

54 A. K. Soper, *RAL Rep*, RAL-TR, 2011-2013.

55 D. A. Keen, A comparison of various commonly used correlation functions for describing total scattering, *J. Appl. Crystallogr.*, 2001, **34**, 172–177.

56 B. Ravel, M. A. Newville and H. Artemis, Data Analysis for X-Ray Absorption Spectroscopy Using IFEFFIT, *J. Synchrotron Radiat.*, 2005, **12**, 537–541.

57 M. Newville, EXAFS Analysis Using FEFF and FEFFIT, *J. Synchrotron Radiat.*, 2001, **8**, 96–100.

58 V. Cuartero, J. García, G. Subías, J. Herrero-Martín, J. Blasco and C. R. Natoli, Origin of Incommensurate Satellite Reflections on $TbMnO_3$ by Resonant X-Ray Scattering, *J. Phys.:Conf. Ser.*, 2013, **430**, 012101.